JOURNAL OF SYNCHROTRON RADIATION

ISSN 1600-5775

Received 27 January 2018
Accepted 11 September 2018

Edited by M. Eriksson, Lund University, Sweden

‡ These authors contributed equally to this work.

Keywords: synchrotron radiation; soft X-ray interference lithography beamline; spatial coherence; wave optics; mutual optical intensity.

The wave optical whole process design of the soft X-ray interference lithography beamline at SSRF

Chaofan Xue,[a]‡ Xiangyu Meng,[a,b]‡ Yanqing Wu,[a]* Yong Wang,[a]* Liansheng Wang,[a] Shumin Yang,[a] Jun Zhao[a] and Renzhong Tai[a]*

[a]Shanghai Institute of Applied Physics, Chinese Academy of Sciences, Shanghai Synchrotron Radiation Facility, Shanghai 201800, People's Republic of China, and [b]University of Chinese Academy of Sciences, Beijing 100049, People's Republic of China. *Correspondence e-mail: wuyanqing@sinap.ac.cn, wangyong@sinap.ac.cn, tairenzhong@sinap.ac.cn

A new spatially coherent beamline has been designed and constructed at the Shanghai Synchrotron Radiation Facility. Here, the design of the beamline is introduced and the spatial coherence is analyzed throughout the whole process by wave optics. The simulation results show good spatial coherence at the endstation and have been proven by experiment results.

1. Introduction

In recent years, soft X-ray interference lithography (XIL) has emerged as a promising tool for academic and industrial research, owing to its high resolution, well defined aerial image, high throughput and large-area capabilities. Large-area high-resolution periodic nanostructures prepared by this technique have been provided to various academic researchers in many scientific research fields such as nanomagnetics (Heyderman *et al.*, 2004), nano-optics (Ekinci *et al.*, 2006), nano-device fabrication (Solak *et al.*, 2004), *etc*. In industrial research, XIL is a powerful and cost-effective tool for extreme ultraviolet (EUV) photoresist testing (Gronheid *et al.*, 2006; Goethals *et al.*, 2006; Ekinci *et al.*, 2012, 2013). The performance of the photoresist is determined by the trade-off in resolution (half-pitch), sensitivity (dose) and line-edge roughness. XIL is a unique technique that can be used to evaluate these three factors simultaneously by one exposure. As a result of its excellent performance, several XIL instruments have been constructed to date at different synchrotron radiation facilities (Ekinci *et al.*, 2013; Shiotani *et al.*, 2008; Isoyan *et al.*, 2008; Lin *et al.*, 2011; Yang *et al.*, 2015).

In XIL, two or more diffracted beams produced by the mask will interfere with each other and the interference fringes are recorded by the photoresist. In a manner of speaking, the success or failure of the experiment depends on the spatial coherence of the light beam. Therefore, it is necessary to analyze the spatial coherence of the light beam delivered by the beamline. Thanks to the rapid development of new coherent sources such as the diffraction-limited storage-ring, the free-electron laser, *etc.*, many models have been developed to satisfy the requirement of analyzing the coherence propagation in synchrotron beamlines (Rio *et al.*, 2011; Osterhoff & Salditt, 2011; Río, 2013; Samoylova *et al.*, 2011; Chubar, 2014; Landau & Lifshitz, 1980; Shi *et al.*, 2014; Meng *et al.*, 2015). A mutual optical intensity (MOI) model has recently been developed to analyze the propagation of partial coherence through a synchrotron beamline (Meng *et*

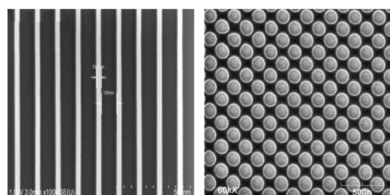

© 2018 International Union of Crystallography

al., 2015). The MOI model is based on statistical theory and uses the mutual optical intensity to describe the coherence property. In addition to providing intensity profiles, the MOI model can be used to calculate the wavefront and the local coherence degree at any location along the beamline. These advantages make the MOI model a powerful tool for beamline design and optimization.

Beamline BL08U at the Shanghai Synchrotron Radiation Facility (SSRF) consists of two branches: BL08U1A for scanning transmission X-ray microscopy (STXM) (Xue *et al.*, 2010) and BL08U1B for XIL (Yang *et al.*, 2015). The XIL branch covers an energy range from 85 eV to 150 eV and shares the undulator source with the STXM branch. The spatial coherence of the delivered light beam can be well controlled by adjusting the exit-slit size. At the end of the beamline, an endstation is designed for XIL as well as other experiments that require a spatially coherent X-ray beam. In this paper, the design and performance of the XIL beamline is described, focusing on the spatial coherence analyzed by the MOI model.

2. Beamline design

2.1. Design principle

The design of a branch beamline is limited by many boundary conditions such as the source parameter, the requirements of the endstation, convenient switching between the main and branch beamline, the spatial layout and so on. For the XIL beamline, major considerations are as follows: (i) the current STXM beamline cannot be disturbed by the XIL beamline and (ii) the beamline design has to satisfy the requirements of the diffraction XIL. The basic requirement for diffraction XIL is a large enough coherent illumination area on the mask and the intensity distribution in the illumination area should be symmetrical. On this premise, the intensity distribution should be as uniform as possible. Higher photon flux is quite important for XIL because it means a shorter exposure time, which helps to reduce the stability requirements of the exposure system. In addition, to keep a good spatial coherence on the mask plane, no reflecting mirrors are allowed after the secondary source (exit slit). The XIL beamline is designed according to the above principles and the total length of the beamline (from the source to the endstation) must be less than 40 m according to the existing layout.

2.2. Beamline layout and phase-space matching

A 4.2 m-long APPLE-II type elliptically polarized undulator with 100 mm periods is employed to produce high-brilliance EUV/soft X-ray photons. The photon energy is chosen by changing the gap distance between the upper and lower pairs of magnet rows. The fundamental wave could cover the required photon energy range 85–150 eV for the XIL experiments. The photon energy was calibrated by the aid of a calibrated monochromator in the BL08U1A branch, because there is no monochromator mounted in the XIL branch. A higher photon energy can also be obtained by adopting a larger undulator gap for experiments other than XIL.

The beamline layout is shown in Fig. 1. After the undulator source, a four-blade aperture (S1) located 20 m from the source point is employed to define the acceptance angle of the beamline. The aperture shared with the BL08U1A branch also functions to absorb most of the heat load and protect the downstream optical elements. There is no monochromator, only two Au-coated cylindrical mirrors mounted in the beamline to focus the beam at the exit slit. The two mirrors are water-side cooled and placed vertically. There are many advantages of placing the two mirrors vertically such as easier switching of the beam between the main and branch beamline as well as minimizing the influence of gravity on the mirror surface. To obtain a uniform spot on the mask, the divergence angles of the horizontal and vertical directions have to be the same. Because the divergence angle is larger in the horizontal direction, the first cylindrical mirror (CM1) is chosen to focus the beam in the horizontal direction, and the second cylindrical mirror (CM2) in the vertical direction at the exit slit (S2). The photon beam can be switched between the two branches simply by moving CM1 in or out of the beam path. Besides deflecting the beam, this mirror plays another role in cutting high-order harmonics. CM2 deflects the beam with a larger

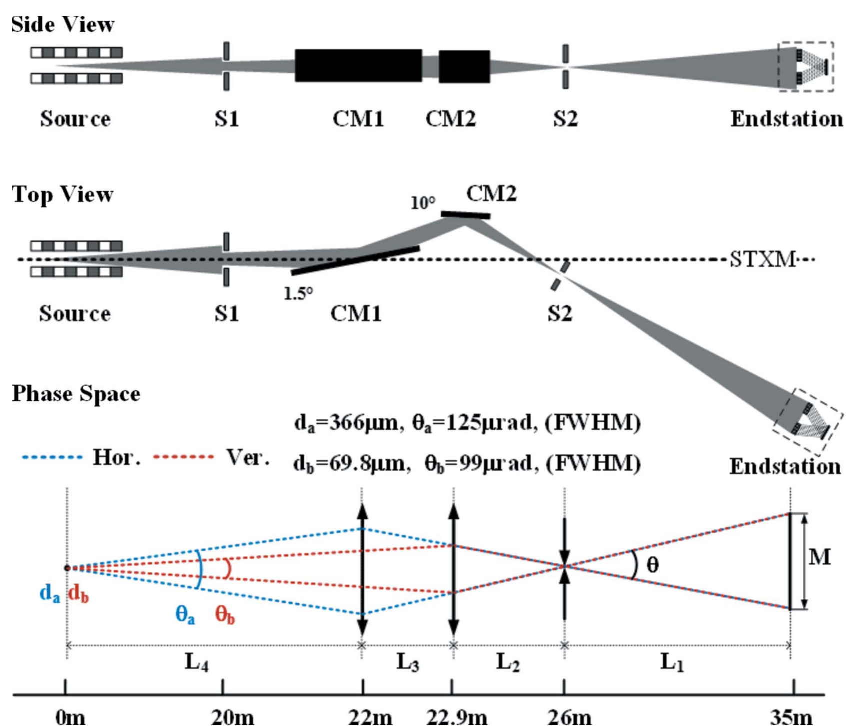

Figure 1
Optical schematic of the BL08U1B beamline.

angle and cuts the rest of the high-order harmonics. The photon beam through the exit slit acts as the direct source to the endstation. By adjusting the size of the exit slit, its spatial coherence can be controlled.

Beam sizes and divergences could be calculated from the vector sum of the electron beam RMS values (σ_x, σ_x', σ_y, σ_y') on the orbit and the radiation values (σ_r, σ_r'). The radiation values are calculated using the approximations $\sigma_r = [(2\lambda L)^{1/2}/2\pi]$ and $\sigma_r' = (\pi/2L)^{1/2}$, where λ is the wavelength of the radiation and L is the length of the insertion device. For the XIL beamline, the calculated beam size and divergence at 92.5 eV are 366 µm and 125 µrad in the horizontal direction and 69.8 µm and 99 µrad in the vertical direction. These divergence angles are less than the receiving angle of the four-blade aperture, so the beamline could receive all of the useful photons produced by the undulator. According to the existing hutch structure, L_4 (the distance between source and CM1) can be fixed to be 22 m and L_3 (the distance between CM1 and CM2) can be fixed to 0.927 m, with grazing-incidence angles of 1.5° for CM1 and 10° for CM2. Other parameters have to be fixed by considering other boundary conditions such as:

(i) Horizontal focus of CM1,

$$\frac{1}{L_4} + \frac{1}{L_2 + L_3} = \frac{2}{R\cos\theta_1}.$$

(ii) Vertical focus of CM2,

$$\frac{1}{L_2} + \frac{1}{L_4 + L_3} = \frac{2\cos\theta_2}{\rho}.$$

(iii) The same divergence angle in two directions after the exit slit,

$$\frac{\theta_a L_4}{L_2 + L_3} = \frac{\theta_b (L_3 + L_4)}{L_2}.$$

(iv) Spot size on the mask,

$$L_1 \frac{\theta_a L_4}{L_2 + L_3} = S_1.$$

(v) Total length of the beamline,

$$L_1 + L_2 + L_3 + L_4 \le 40.$$

Here, R and ρ are the respective radii of CM1 and CM2, θ_1 and θ_2 are the grazing incidence angles of CM1 and CM2, L_2 is the distance between the exit slit and CM2, L_1 is the distance between the exit slit and the mask, and S_1 is the spot size on the mask. To guarantee a 4 mm × 4 mm coherent illumination area on the mask, S_1 is set to 6 mm. Finally, four unknown parameters L_1, L_2, R and ρ could be determined by combining the above boundary conditions. According to our calculation results, the mask is placed 34.989 m from the source, and the divergence angle after the exit slit is 0.6688 mrad. The main optical parameters of the XIL beamline are listed in Table 1.

2.3. Optical efficiency and photon flux

Higher photon flux on the mask means shorter exposure time, which is quite important for XIL experiments because it helps to diminish vibrational effects. Since only two mirrors are employed in the beamline, a higher reflectivity could be obtained. The XIL experiment is usually carried out at 92.5 eV and 140 eV at SSRF and the calculated reflectivity of the fundamental harmonic is greater than 60% at these energy points (shown in Fig. 2) where both mirrors are coated by 50 nm-thick gold.

The reflectivity plays an important role in beamline efficiency, but the final photon flux that arrives at the mask is not soley decided by the reflectivity. There are many other factors that affect the photon flux such as source brightness and the actual size of the aperture or slit. Because the high coherence property is important in the XIL experiments, the spot size at the exit slit is decreased by closing this slit to improve coherence. Besides, the size of the aperture or slit is also adjusted to optimize the uniformity and symmetry of the spot on the mask. Taking these factors into account, the calculated photon flux of the fundamental harmonic is shown in Fig. 3(*a*). The photon flux is characterized by an AXUV100G photodiode in front of the mask through measuring the photocurrent. The measured results show that a photon flux larger than 10^{14} photons s^{-1} was achieved over the entire range. The spectral purity of the photon beam in the endstation is shown in Fig. 3(*b*). Though there is no monochromator mounted on the beamline, the proportion of higher-order harmonics is almost less than 10%. The dose contributed by such a small amount of higher-order harmonics is outside the process window (Zhao *et al.*, 2017) and will not affect the exposure result.

Table 1
Main optical parameters of the XIL beamline.

Parameter	Value
Distance between source and CM1 (L_4)	22 m
Distance between CM1 and CM2 (L_3)	0.927 m
Distance between CM2 and exit slit (L_2)	3.0904 m
Distance between exit slit and mask (L_1)	8.9717 m
Grazing incidence angle of CM1 (θ_1)	1.5°
Grazing incidence angle of CM2 (θ_2)	10°
Radius of curvature of CM1 (R)	259.5488 m
Radius of curvature of CM2 (ρ)	0.9458 m

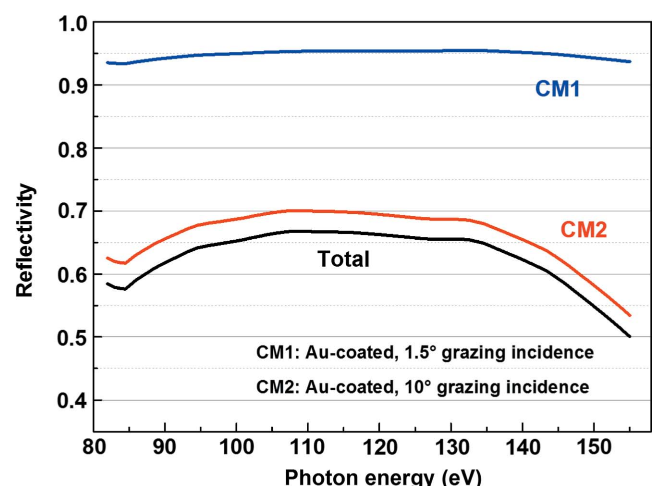

Figure 2
The mirror reflectivity of the beamline.

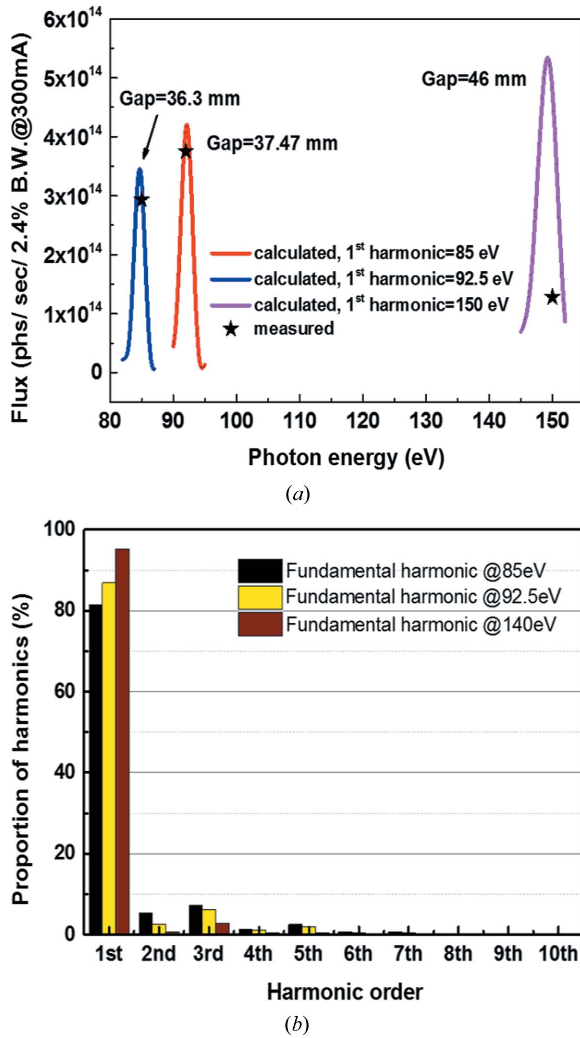

Figure 3
(*a*) Calculated and measured photon flux at the mask normalized to a beam current of 300 mA. (*b*) Spectral purity of the photon beam at the endstation.

2.4. XIL endstation

An XIL system consisting of an interferometer (mask) sample module, order-sorting aperture (OSA) module and detector was permanently installed at the endstation in a 100-class clean room. A transmission diffraction-type grating was chosen for the mask in order to produce multi-coherent beams. The angle of the mask could be adjusted up–down and right–left to guarantee that the incoming beam is perpendicular to the mask to eliminate phase errors. In addition, the mask can be also moved along the beam direction to adjust the distance between the mask and the sample, which is decided by many factors such as photon wavelength, mask period, mask area *etc*. The sample is integrated with the mask in the same module to eliminate the vibration between them. An OSA is added in the XIL system to block the zeroth-order diffraction from the mask grating for stitching the exposure area together (Xue *et al.*, 2016). A CCD camera is mounted at the end of the chamber to observe the uniformity of illumination on the mask grating and to align the OSA and the mask grating *in situ*. Besides XIL, this CCD camera can also act as a detector in other experiments that require a spatially coherent X-ray beam such as coherent diffraction imaging.

3. Spatial coherence analysis

3.1. Partially coherent beam propagation

In this section, the mutual optical intensity (MOI) model is used to analyze partially coherent X-ray propagation in the horizontal direction through the XIL beamline. The MOI model is used to describe the coherence properties in this paper. When the X-ray source has a narrow angular divergence, the MOI can be expressed by a Gaussian-shell model (Vartanyants & Singer, 2010; Pelliccia *et al.*, 2011) for simplification,

$$J(x_1, y_1, x_2, y_2) = \left[I(x_1, y_1)\right]^{1/2}\left[I(x_2, y_2)\right]^{1/2}\mu(x_1, y_1, x_2, y_2), \quad (1)$$

where

$$I(x, y) = I_0 \exp\left(-\frac{x^2}{2\sigma_x^2} - \frac{y^2}{2\sigma_y^2}\right), \quad (2)$$

$$\mu(x_1, y_1, x_2, y_2) = \exp\left[-\frac{(x_2 - x_1)^2}{2\xi_x^2} - \frac{(y_2 - y_1)^2}{2\xi_y^2}\right], \quad (3)$$

where I and μ are the intensity and coherence degree and σ and ξ are the spot size and the transverse coherence length, respectively. At 92.5 eV, the source size σ and the coherence length ξ are calculated to be 155 µm and 41.6 µm in the horizontal direction, respectively.

The intensity and coherence-degree profiles at specific locations are shown in Fig. 4. The coherence degree μ is defined between any point and the central point. Figs. 4(*a*) and 4(*b*) show the intensity and coherence degree at the four-blade aperture plane. The wavefront is not cut when propagating from the source to the aperture such that it is diffraction-free propagation. Therefore, both intensity and coherence profiles maintain good Gaussian shapes. The spot size and coherence length at the four-blade aperture plane are calculated to be 1046 µm and 281 µm, respectively.

The four-blade aperture is chosen to be 1100 µm and the beam is limited by this aperture because the beam size has diverged to 4184 µm (4σ). The intensity and coherence-degree profiles at the incident plane of the first cylinder mirror are acquired, as shown in Figs. 4(*c*) and 4(*d*). The intensity profile coincides with Fresnel diffraction while the coherence degree profile has apparent oscillations at the edges. This phenomenon originates from the finite acceptance of the four-blade aperture. A coherence length of 312 µm can be obtained by Gaussian fitting of the central peak of the coherence-degree profile.

The first cylinder mirror focuses the beam horizontally onto the exit-slit plane. The intensity and coherence degree profiles are shown in Figs. 4(*e*) and 4(*f*), respectively. Despite the four-blade aperture cutting the beam, the intensity profile at the exit plane remains in a Gaussian distribution. However, the

Table 2
Beam size and coherence length at different positions.

Position	Beam size (μm, 4σ)	Coherence length (μm)
Source	620	41.6
Four-blade aperture	4184	281
Exit slit	132.4	29.6
Endstation	1245	3889

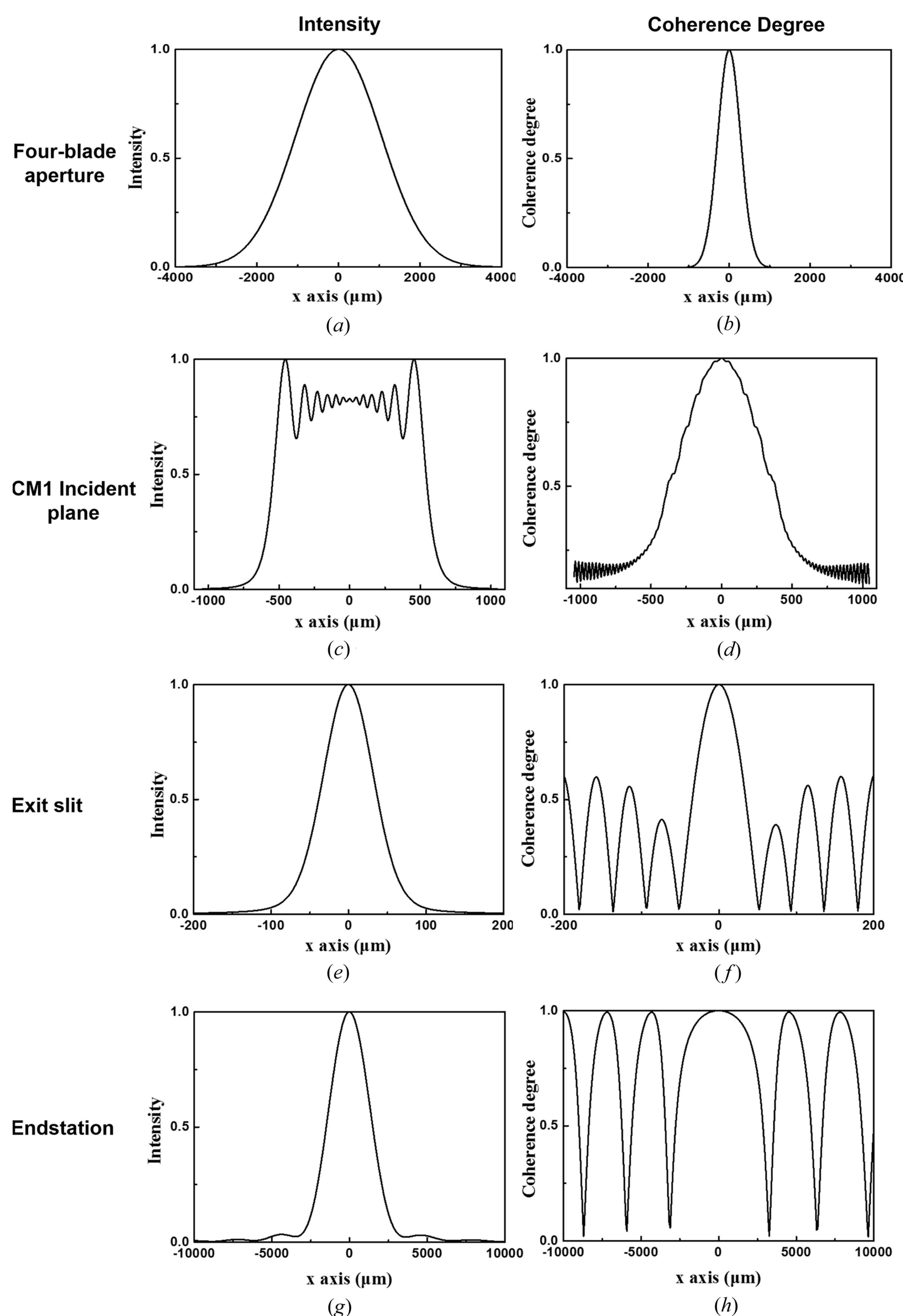

Figure 4
(a) Normalized intensity and (b) coherence-degree profiles at the four-blade aperture (S1); (c) and (d) the incident plane of the first cylindrical mirror (CM1); (e) and (f) the exit slit (S2); and (g) and (h) the endstation. The intensity profiles are shown in (a), (c), (e) and (g) and the coherence degrees are shown in (b), (d), (f) and (h). The coherence degree is defined between any point and the central point.

coherence-degree profile has clear oscillations that can be attributed to diffraction by the four-blade aperture. A spot size of 33.1 μm and coherence length of 29.6 μm can be obtained at the exit-slit plane by fitting the central profiles.

The beam would be limited if a 40 μm exit slit is chosen because the focal spot is 132.4 μm (4σ). The exit slit is composed of two pairs of blades which are not in the same plane. The upstream pairs are placed vertically to limit the vertical size of the spot and the downstream pairs are placed horizontally to limit the horizontal size of the spot. There is a 4 mm gap between the two pairs of blades along the optical axis and the effect of the gap has already been considered in the propagation through the exit slit. As a result of the Fraunhofer diffraction from the limited exit slit, the intensity profile at the endstation has some diffraction peaks, as shown in Fig. 4(g). The −1st-order peak is located at x = −4385 μm with an amplitude of 0.034, while the 1st-order peak is located at x = 4518 μm with an amplitude of 0.031. The asymmetry distribution can also be found in the ±2nd-order diffraction and is mainly caused by the gap between the two blades. Because the gap is 4 mm long, which is greater than the wavelength of 13.5 nm, the wavefront propagation from the front blade to the back blade can be seen as a single-side diffraction. The second single-side diffraction is generated by the back blade which also acts to block another side of the wavefront from passing through the exit slit. There are two single-side diffractions occurring one after the other, which generate an asymmetric intensity distribution at the endstation. Moreover, the coherence degree also has an asymmetric distribution for the same reason, as shown in Fig. 4(h). The coherence length at the endstation is calculated to be 3889 μm, which is greater than the beam size of 1245 μm. Therefore, the beam at the endstation can be considered fully coherent X-ray. The beam size and the coherence length at different positions are listed in Table 2.

3.2. Coherence optimization

For the XIL setup, the coherent beam is diffracted by mask gratings firstly, and then the diffraction beams interfere to generate a standing wave

pattern. This pattern can be projected as an aerial image onto the exposure area. Therefore, to produce periodic patterns the spatially coherent illumination is quite important in the XIL. Though the coherence can be improved by reducing the beam size, photon flux will also be lost at the same time. Less flux means longer exposure times, which amplifies the vibrational effects. The balance between coherence and flux is very important for improving the quality of the exposure patterns.

When the four-blade aperture is set to 1100 µm and the exit slit is set to 80 µm, the spot size and coherence length are calculated to be 1085 µm and 1325 µm at the endstation, respectively. There are two amplitude gratings horizontally installed at the endstation to manufacture an aerial image. The interference pattern produced by X-ray lithography with partially coherent light can also be simulated by the MOI model. The size of the amplitude grating is chosen to be 400 µm, with a 280 nm period and 0.5 duty circle. The photon stop is 600 µm long and blocks the photons passing through the gratings directly. The fringe-intensity distribution at the exposure area is calculated using the MOI model, as shown in Fig. 5(*a*). There are some slight intensity oscillations, which originate from the Fresnel diffraction by the finite-grating modelling as a single aperture. However, the fringe period and visibility values remain at 0.14 µm and 0.75 ± 0.01 within the whole exposure area. To optimize the XIL beamline, the flux and fringe visibility at the exposure area were calculated with varying exit-slit size, as shown in Fig. 5(*b*). The normalized flux (black markers) increases non-linearly *versus* the exit-slit size. Due to the beam size 4σ of 156 µm at the exit slit plane, the normalized flux reaches the approximate maximum of 1 when the exit-slit size is increased up to 155 µm. On the other hand, the fringe visibility (blue markers) decreases non-linearly *versus* the exit-slit size. When the exit-slit size is greater than 155 µm, the fringe visibility reaches a low limit of 0.33, due to the finite four-blade aperture of 1100 µm. For the manufacture of high-quality patterns, the exit slit is limited to 50 µm; the fringe visibility is increased to 0.94 and the normalized flux is reduced to 0.41.

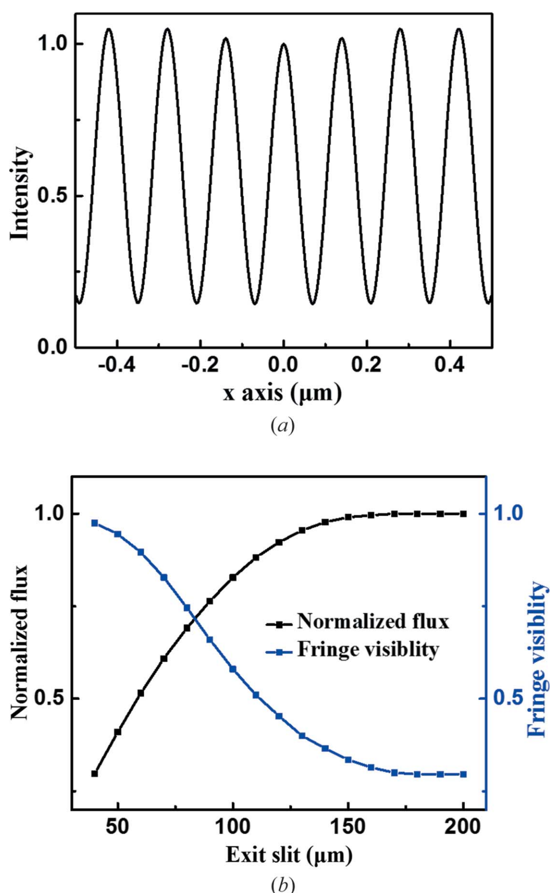

Figure 5
(*a*) Fringe-intensity profile at the exposure area; (*b*) normalized flux and fringe visibility at the exposure area with a variable exit slit.

4. Experimental results and discussion

4.1. Coherence length measurement

There are many techniques for the measurement of X-ray coherence length, including Young's double-slit diffraction and grating interferometry. In this paper, a beam position monitor (BPM) was applied to detect the Fraunhofer diffraction caused by the exit slit. To verify the experimental results, the MOI model was used to obtain the intensity distribution diffracted by the exit slit. By comparing the experimental and theoretical results, the coherence length at the BPM position could be obtained.

The BPM was composed of two carbon wires to generate photoelectrons when the wires were irradiated by X-rays. The beam intensity distribution could be finally acquired by detecting the photoelectron. For acquiring good coherence properties, the four-blade aperture and exit slit were chosen to be 1100 µm and 40 µm, respectively, just as the actual size in the XIL experiments. The BPM is located 4.6 m downstream from the exit slit. The intensity profile was obtained by scanning the BPM within the range −9 mm to 9 mm with steps of 0.24 mm. Fig. 6(*a*) shows the experimental intensity profile detected by the BPM and the theoretical intensity profile calculated using the MOI model. When the exit-slit sizes were 25 µm, 35 µm, 40 µm and 45 µm, the experimental and theoretical results always coincided with each other. This indicated that the MOI model is suitable for the simulation of X-ray propagation through beamlines. The gap between the two blades generated the intensity asymmetry distribution, which decreased with increasing exit-slit size. A spot size of 594 µm could be obtained by Gaussian fitting the intensity profile for an exit slit of 40 µm. The corresponding coherence-degree profile is shown in Fig. 6(*b*). The coherence length was found to be about 2915 µm by fitting the central peak. Since the coherence length was much greater than the spot size, the beam could be seen as a fully coherent X-ray. The fringe-intensity profile at the exposure area was calculated using the MOI model, as shown in Fig. 6(*c*). Owing to an approximately full coherence, the fringe visibility reaches up to 0.98.

4.2. XIL exposure

The X-ray interference lithography endstation mounted at the end of beamline BL08U1B is devoted to obtaining peri-

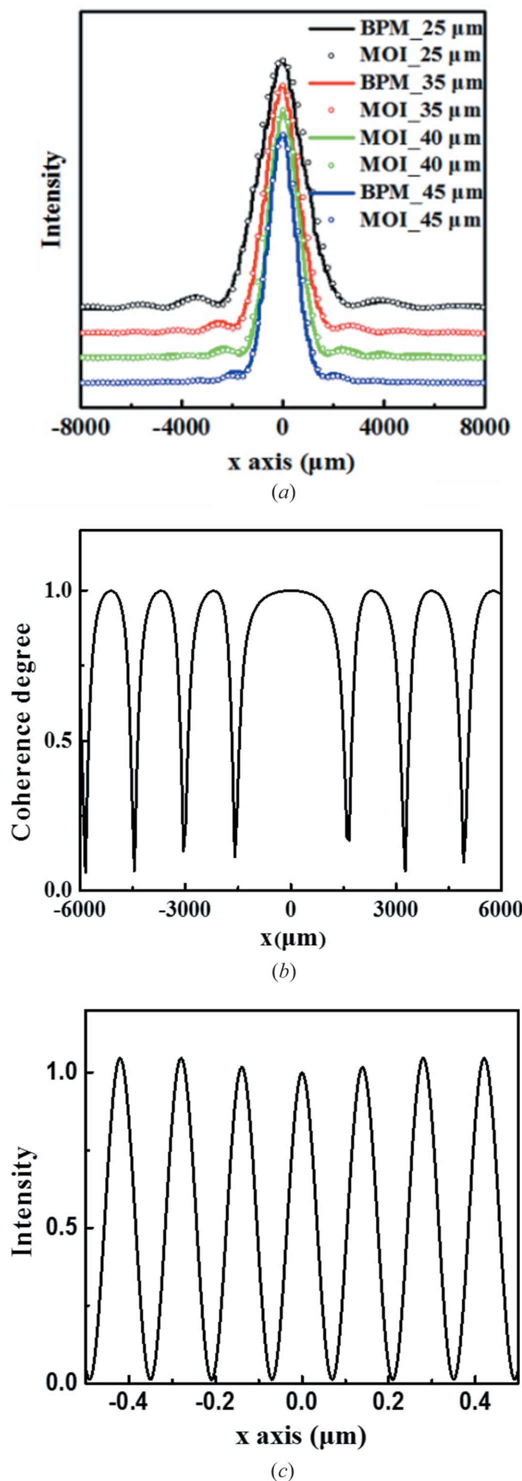

Figure 6
(*a*) Intensity profiles at the BPM position with different exit-slit sizes; the curves are experimental results obtained by BPM scanning and the dots are simulation results obtained using the MOI model. (*b*) Coherence-degree profile at the BPM position. (*c*) Fringe-intensity profile at the exposure area, both at an exit-slit size of 40 µm.

odic nanostructures. The incoming beam is diffracted by a transmission diffraction-type multi-grating mask to produce two or more coherent EUV beams. Finally, the interference pattern of the coherent multi-beams is recorded on the

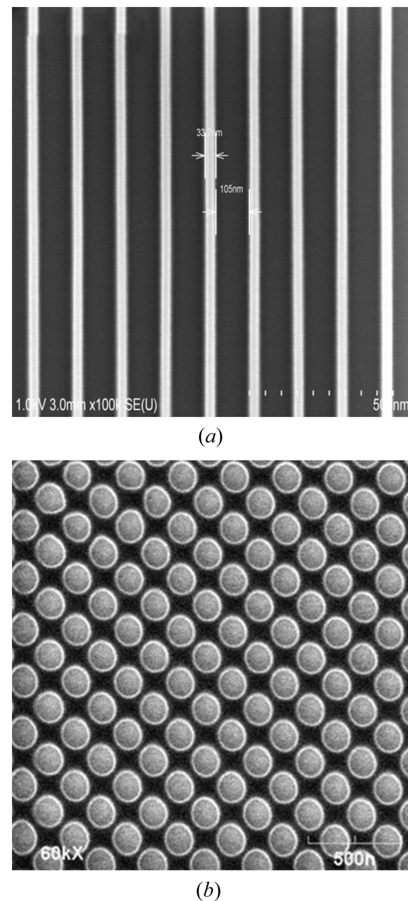

Figure 7
Exposure results of the XIL beamline: (*a*) line structures with a period of 140 nm on the user's molecular glass photoresist obtained by adopting a two-grating mask with a grating period of 280 nm. (*b*) Periodic nanoholes with a period of 200 nm on the PMMA photoresist obtained by adopting a four-grating mask with a grating period of 280 nm.

photoresist. The pattern shape and period is decided by the grating mask. Fig. 7 shows the exposure results by adopting a two-grating mask and a four-grating mask, respectively, where the grating period is 280 nm. The exposure result with the two-grating mask is shown in Fig. 7(*a*). A line structure with a 140 nm period is obtained on a self-developed molecular glass photoresist by users who concentrate on EUV photoresist development (Chen *et al.*, 2014). Fig. 7(*b*) shows a 200 nm period nanohole structures on the polymethyl methacrylate (PMMA) photoresist (Zhao *et al.*, 2017), which is obtained by adopting the four-grating mask. The periods of both patterns are consistent with the theoretical simulation results whereas the duty cycle is not strictly consistent with theoretical predictions. This is mainly caused by the exposure doses. A large dose means that more photons will participate in the exposure, thus the lines on the photoresist will be finer. However, the period of the pattern will not be changed under different doses.

Aside from the period, another key parameter of the pattern is height, which is quite important for both science and pattern-transfer processing. Fundamentally, the fringe visibility determines the exposure height of the nanostructure, though the height also depends on many other factors such as

the transmission rate. The calculated result in Fig. 6(*c*) shows that the fringe visibility could reach up to 0.98, which guarantees a large depth structure. Unfortunately, the exposure results are difficult to reflect in the fringe visibility directly because the height of the nanostructure is also affected by many other factors such as the transmission rate and the exposure dose as mentioned above. However, many high-aspect-ratio periodic nanostructures have been obtained (Zhao *et al.*, 2017; Xue *et al.*, 2017) in the XIL endstation, which provides evidence of good coherence.

5. Summary

The design and construction of a new soft X-ray interference lithography beamline at SSRF is introduced in this work. The spatial coherence is analyzed by the newly developed mutual optical intensity model and verified by experimental results. The beamline has been opened to users since January 2013. To date, many research results in both scientific and industrial fields have been obtained based on the high-quality spatially coherent light beams delivered by the beamline.

Acknowledgements

The authors wish to thank the staff of the BL08U beamline at SSRF.

Funding information

This work was supported by National Key R&D Program of China (2017YFA0206001), the National Natural Science Foundation of China (grant Nos. 11775291, 11505275, 11475251, 11275255, Y615301061), the Youth Innovation Promotion Association (grant No. 2017306), the Open Research Project of Large Scientific Facility from Chinese Academy of Sciences: Study on Self-Assembly Technology and Nanometer Array with Ultrahigh Density.

References

Chen, L., Xu, J., Yuan, H., Yang, S. M., Wang, L. S., Wu, Y. Q., Zhao, J., Chen, M., Liu, H. G., Li, S. Y., Tai, R. Z., Wang, S. Q. & Yang, G. Q. (2014). *Sci. China Chem.*, **57**, 1746–1750.

Chubar, O. (2014). *Proc. SPIE*, **9209**, 920907.

Ekinci, Y., Solak, H. H., David, C. & Sigg, H. (2006). *Opt. Express*, **14**, 2323–2334.

Ekinci, Y., Vockenhuber, M., Hojeij, M., Wang, L. & Mojarad, N. M. (2013). *Proc. SPIE*, **8679**, 867910.

Ekinci, Y., Vockenhuber, M., Terhalle, B., Hojeij, M., Wang, L. & Younkin, T. R. (2012). *Proc. SPIE*, **8322**, 83220W.

Goethals, A. M., Gronheid, R., Van Roey, F., Solak, H. H. & Ekinci, Y. (2006). *J. Photopol. Sci. Technol.* **19**, 501–506.

Gronheid, R., Solak, H. H., Ekinci, Y., Jouve, A. & Van Roey, F. (2006). *Microelectron. Eng.* **83**, 1103–1106.

Heyderman, L. J., Solak, H. H., David, C., Atkinson, D., Cowburn, R. P. & Nolting, F. (2004). *Appl. Phys. Lett.* **85**, 4989–4991.

Isoyan, A., Wüest, A., Wallace, J., Jiang, F. & Cerrina, F. (2008). *Opt. Express*, **16**, 9106–9111.

Landau, L. D. & Lifshitz, E. M. (1980). *The Classical Theory of Fields*. Burlington, MA: Butterworth & Heinemann.

Lin, C.-H., Fong, C.-H., Lin, Y.-M., Lee, Y.-Y., Fung, H.-S., Shew, B.-Y. & Shieh, J. (2011). *Microelectron. Eng.* **88**, 2639–2641.

Meng, X., Xue, C., Yu, H., Wang, Y., Wu, Y. & Tai, R. (2015). *Opt. Express*, **23**, 29675.

Osterhoff, M. & Salditt, T. (2011). *New J. Phys.* **13**, 103026.

Pelliccia, D., Nikulin, A. Y., Moser, H. O. & Nugent, K. A. (2011). *Opt. Express*, **19**, 8073–8078.

Río, M. S. del (2013). *J. Phys. Conf. Ser.* **425**, 162003.

Samoylova, L., Buzmakov, A., Geloni, G., Chubar, O. & Sinn, H. (2011). *Proc. SPIE*, **8141**, 81410A.

Sanchez del Rio, M., Canestrari, N., Jiang, F. & Cerrina, F. (2011). *J. Synchrotron Rad.* **18**, 708–716.

Shi, X., Reininger, R., Sanchez del Rio, M. & Assoufid, L. (2014). *J. Synchrotron Rad.* **21**, 669–678.

Shiotani, H., Suzuki, S., Lee, D. G., Naulleau, P., Fukushima, Y., Ohnishi, R., Watanabe, T. & Kinoshita, H. (2008). *Jpn. J. Appl. Phys.* **47**, 4881–4885.

Solak, H. H., David, C. & Gobrecht, J. (2004). *Appl. Phys. Lett.* **85**, 2700–2702.

Vartanyants, I. A. & Singer, A. (2010). *New J. Phys.* **12**, 035004.

Xue, C. F., Wang, Y., Guo, Z., Wu, Y. Q., Zhen, X. J., Chen, M., Chen, J. H., Xue, S., Peng, Z. Q., Lu, Q. P. & Tai, R. Z. (2010). *Rev. Sci. Instrum.* **81**, 103502.

Xue, C., Wu, Y., Zhu, F., Yang, S., Liu, H., Zhao, J., Wang, L. & Tai, R. (2016). *Rev. Sci. Instrum.* **87**, 043303.

Xue, C., Zhao, J., Wu, Y., Yu, H., Yang, S., Wang, L., Zhao, W., Wu, Q., Zhu, Z., Liu, B., Zhang, X., Zhou, W. & Tai, R. (2017). *Appl. Surf. Sci.* **425**, 553–557.

Yang, S.-M., Wang, L.-S., Zhao, J., Xue, C.-F., Liu, H.-G., Xu, Z.-J., Wu, Y.-Q. & Tai, R.-Z. (2015). *Nucl. Sci. Tech.* **26**, 010101.

Zhao, J., Wu, Y., Xue, C., Yang, S., Wang, L., Zhu, F., Zhu, Z., Liu, B., Wang, Y. & Tai, R. (2017). *Microelectron. Eng.* **170**, 49–53.